PERGAMON

Journal of Quantitative Spectroscopy &
Radiative Transfer 63 (1999) 409–432

Journal of
Quantitative
Spectroscopy &
Radiative
Transfer

www.elsevier.com/locate/jqsrt

Bidirectional reflectance of flat, optically thick particulate layers: an efficient radiative transfer solution and applications to snow and soil surfaces

Michael I. Mishchenko[a,]*, Janna M. Dlugach[b], Edgard G. Yanovitskij[b],
Nadia T. Zakharova[c]

[a]*NASA Goddard Institute for Space Studies, 2880 Broadway, New York, NY 10025, USA*
[b]*Laboratory for Radiative Transfer Theory, The Main Astronomical Observatory,*
Ukrainian National Academy of Sciences, Golosiiv, 252650 Kyiv-22, Ukraine
[c]*Science Systems and Applications, Incorporated, 2880 Broadway, New York, NY 10025, USA*

Abstract

We describe a simple and highly efficient and accurate radiative transfer technique for computing bidirectional reflectance of a macroscopically flat scattering layer composed of nonabsorbing or weakly absorbing, arbitrarily shaped, randomly oriented and randomly distributed particles. The layer is assumed to be homogeneous and optically semi-infinite, and the bidirectional reflection function (BRF) is found by a simple iterative solution of the Ambartsumian's nonlinear integral equation. As an exact solution of the radiative transfer equation, the reflection function thus obtained fully obeys the fundamental physical laws of energy conservation and reciprocity. Since this technique bypasses the computation of the internal radiation field, it is by far the fastest numerical approach available and can be used as an ideal input for Monte Carlo procedures calculating BRFs of scattering layers with macroscopically rough surfaces. Although the effects of packing density and coherent backscattering are currently neglected, they can also be incorporated. The FORTRAN implementation of the technique is available on the World Wide Web at http://www.giss.nasa.gov/ ~ crmim/brf.html and can be applied to a wide range of remote sensing, engineering, and biophysical problems. We also examine the potential effect of ice crystal shape on the bidirectional reflectance of flat snow surfaces and the applicability of the Henyey–Greenstein phase function and the δ-Eddington approximation in calculations for soil surfaces. © 1999 Elsevier Science Ltd. All rights reserved.

---

* Corresponding author. Tel.: + 212-678-5590; fax: + 212-678-6522
E-mail address: crmim@giss.nasa.gov (M.I. Mishchenko)

0022-4073/99/$ - see front matter © 1999 Elsevier Science Ltd. All rights reserved.
PII: S0022-4073(99)00028-X

1. Introduction

Many remote sensing, engineering, and biophysical applications rely on accurate knowledge of the bidirectional reflection function (BRF) of layers composed of discrete, randomly positioned scattering particles (e.g., Refs. [1–46]). Theoretical computations of BRFs for plane-parallel particulate layers are usually reduced to solving the radiative transfer equation (RTE) using one of the existing exact or approximate techniques. Since some semi-empirical approximate approaches such as the Hapke model [13] are notorious for their low accuracy, crude violation of the energy conservation law, and ability to produce unphysical results [28,31], the use of numerically exact solutions of RTE has gained justified popularity. For example, the computation of BRFs for particulate layers with macroscopically flat surfaces in Refs. [5,17,19–22] is based on the adding–doubling technique [47,48], while Refs. [9,10] employ the discrete ordinate method [49]. BRF computations for layers with undulated (macroscopically rough) surfaces are more complicated and often may have to rely on time-consuming Monte Carlo procedures. This approach is especially inefficient for optically thick, weakly absorbing media (e.g., snow and desert surfaces at visible wavelengths) since a photon may undergo many internal scattering events before it exits the medium or is absorbed. However, particulate layers with undulated surfaces can often be represented as collections of locally flat tilted facets characterized by the BRF found from the traditional plane-parallel RTE. In this way the Monte Carlo procedure could be used only to evaluate the effects of surface shadowing and multiple surface reflections, thereby bypassing the time-consuming ray tracing inside the medium and providing a great saving of CPU time.

A further saving of computer resources can be achieved by using a more efficient technique for solving the plane-parallel RTE for a semi-infinite medium than the adding/doubling and discrete ordinate methods. Since many natural and artificial particulate layers can be considered optically semi-infinite and homogeneous, one can find the BRF directly by solving the Ambartsumian's nonlinear integral equation [50] using a simple iterative technique [51,52]. In this way, the computation of the internal radiation field is avoided (cf. Refs. [47–49]) and the computer code becomes highly efficient and very accurate and compact. In the following sections, we discuss in detail numerical aspects and the computer implementation of this technique, examine the applicability of the Henyey–Greenstein phase function and the δ-Eddington approximation in BRF and flux calculations for soil surfaces, and describe sample applications demonstrating the potential effect of ice crystal shape on the bidirectional reflectance of flat snow surfaces. The last section summarizes the results of the paper and outlines further potential improvements of the model.

2. Computational technique

We assume that the scattering layer is optically semi-infinite, has a macroscopically flat surface, and is composed of randomly distributed and randomly oriented particles of arbitrary shape. For simplicity, we ignore polarization effects and use intensity as the only physical characteristic of light. This so-called scalar approximation is not necessarily good for Rayleigh scattering [53,54], but appears to be sufficiently accurate for particles with sizes comparable to and larger than the wavelength [55]. To describe the geometry of light scattering, we use a right-handed spherical coordinate system with the z-axis directed along the outward normal to the surface (Fig. 1). The

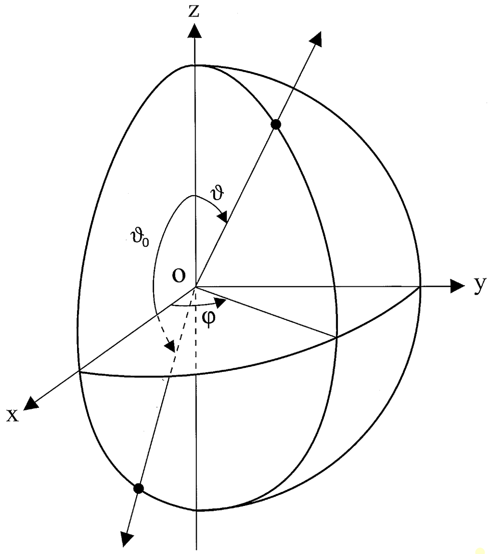

Fig. 1. Spherical coordinates specifying the direction of light propagation. The zenith and azimuth angles of the incident beam are $\vartheta_0 > \pi/2$ and $\varphi_0 = 0$, respectively.

direction of light propagation is specified by the couple (u, φ), where $u = -\cos\vartheta$, $\vartheta \in [0°, 180°]$ is the zenith angle, and $\varphi \in [0°, 360°]$ is the azimuth angle. The azimuth angle is measured in the clock-wise direction when looking in the positive z direction. Note that $u < 0$ for upwelling radiation and $u > 0$ for downwelling radiation. We also define $\mu = |u|$. The surface is illuminated by a beam of unpolarized light incident in the direction $(\mu_0, \varphi_0 = 0)$. The intensity of the reflected radiation is given by

$$I(-\mu, \varphi) = \mu_0 R(\mu, \mu_0, \varphi) F, \tag{1}$$

where $R(\mu,\mu_0,\varphi)$ is the bidirectional reflection function and πF is the incident flux per unit area perpendicular to the incident beam. We ignore the effects of packing density, coherent backscattering, and shadow hiding (see Section 5) and find the reflection function as a numerically exact solution of the conventional radiative transfer equation [50,56]. Specifically, we expand $R(\mu, \mu_0, \varphi)$ in a Fourier series in azimuth,

$$R(\mu, \mu_0, \varphi) = R^0(\mu, \mu_0) + 2 \sum_{m=1}^{m_{\max}} R^m(\mu, \mu_0) \cos m\varphi \tag{2}$$

and solve numerically the Ambartsumian's nonlinear integral equation [50,51]

$$\begin{aligned}(\mu + \mu_0) R^m(\mu, \mu_0) = {} & \frac{\varpi}{4} P^m(-\mu, \mu_0) + \frac{\varpi}{2}\mu_0 \int_0^1 P^m(\mu, \mu') R^m(\mu', \mu_0)\, \mathrm{d}\mu' + \frac{\varpi}{2}\mu \int_0^1 R^m(\mu, \mu') P^m(\mu', \mu_0)\, \mathrm{d}\mu' \\ & + \varpi\mu\mu_0 \int_0^1 \int_0^1 R^m(\mu, \mu') P^m(-\mu', \mu'') R^m(\mu'', \mu_0)\, \mathrm{d}\mu'\, \mathrm{d}\mu'',\end{aligned} \tag{3}$$

where ϖ is the single-scattering albedo and $P^m(\mu,\mu')$ are Fourier components of the phase function:

$$P(\mu,\mu',\varphi-\varphi') = P^0(\mu,\mu') + 2\sum_{m=1}^{m_{\max}} P^m(\mu,\mu')\cos m(\varphi-\varphi'). \tag{4}$$

The upper summation limit in Eq. (2) is chosen such that the absolute numerical accuracy of the Fourier expansion of the reflection function is better than a small predefined number ε (e.g., $\varepsilon = 10^{-4}$).

The Fourier components of the phase function are given by

$$P^m(\mu,\mu') = (-1)^m \sum_{s=m}^{s_{\max}} \alpha_s P^s_{m0}(\mu)P^s_{m0}(\mu'), \tag{5}$$

where $P^s_{mn}(x)$ are generalized spherical functions [57,58] closely related to associate Legendre functions (Section 3.2) and α_s are expansion coefficients appearing in the standard expansion of the phase function $P(\Theta)$ in Legendre polynomials $P_s(x) = P^s_{00}(x)$:

$$P(\Theta) = \sum_{s=0}^{s_{\max}} \alpha_s P_s(\cos\Theta), \quad \alpha_0 \equiv 1, \tag{6}$$

where Θ is the scattering angle and $s_{\max}$ is chosen such that all expansion coefficients with $s > s_{\max}$ are smaller than 0.1ε. Note that $m_{\max} \le s_{\max}$ and we assume the following standard normalization of the phase function:

$$\frac{1}{2}\int_0^\pi P(\Theta)\sin\Theta\,\mathrm{d}\Theta = 1. \tag{7}$$

If the expansion coefficients α_s are known, then one can easily compute the Fourier components of the phase function via Eq. (5) and finally solve Eq. (3) using the method of simple iterations.

It has been found that the method of simple iterations works very well for all $m > 0$. Furthermore, convergence is reasonably fast for $m = 0$ provided that the particles are absorbing ($\varpi < 1$). However, iterations converge very slowly or even may diverge for nonabsorbing or weakly absorbing particles ($1 - \varpi \ll 1$) [51]. It has been proved mathematically that this behavior is explained by the nonuniqueness of solutions of Eq. (3) [59]. To ameliorate this convergence problem, Dlugach and Yanovitskij [51] suggested to modify the $R^m(\mu,\mu_0)$ value after each iteration by enforcing the so-called Sobolev–van de Hulst relation

$$i(-\mu) = 2\int_0^1 R^0(\mu,\mu_0)i(\mu_0)\mu_0\,\mathrm{d}\mu_0. \tag{8}$$

The function $i(u)$ is the solution of the equation

$$i(u)(1-ku) = \frac{\varpi}{2}\int_{-1}^{+1} i(u')P^0(u,u')\,\mathrm{d}u', \tag{9}$$

in which the so-called diffusion exponent k is found by satisfying the normalization condition

$$\frac{\varpi}{2}\int_{-1}^{+1} i(u)\,\mathrm{d}u = 1. \tag{10}$$

After Eq. (3) is solved for each m, the evaluation of the Fourier series of Eq. (2) finalizes the process of computing the reflection function for any μ, μ_0, and φ. This function can then be used to calculate the reflected intensity for any directions of illumination and reflection and to find the plane, $A_{\mathrm{P}}(\mu_0)$, and the spherical, A_{S}, albedos:

$$A_{\mathrm{P}}(\mu_0) = \frac{1}{\pi}\int_0^1 \mathrm{d}\mu\,\mu \int_0^{2\pi} \mathrm{d}\varphi\, R(\mu,\mu_0,\varphi) = 2\int_0^1 R^0(\mu,\mu_0)\mu\,\mathrm{d}\mu, \tag{11}$$

$$A_{\mathrm{S}} = 2\int_0^1 A_{\mathrm{P}}(\mu_0)\mu_0\,\mathrm{d}\mu_0. \tag{12}$$

Note that the BRF thus computed satisfies the fundamental principle of reciprocity:

$$R(\mu,\mu_0,\varphi) = R(\mu_0,\mu,\varphi). \tag{13}$$

Furthermore, since $i(\pm\mu) \equiv 1$ if $\varpi = 1$, enforcing Eq. (8) ensures energy conservation for a semi-infinite nonabsorbing medium by rendering the plane and spherical albedos equal to 1 [cf. Eqs. (8), (11), and (12)].

3. Numerical aspects and computer codes

In this section we discuss numerical aspects and a FORTRAN implementation of the technique briefly outlined in the previous section. All computer procedures described are openly available on the World Wide Web at http://www.giss.nasa.gov/ ~ crmim/brf.html.

3.1. Legendre expansion of the phase function

The widely used Henyey–Greenstein phase function and its Legendre expansion coefficients are given by the following simple formulas:

$$P(\Theta) = \frac{1-g^2}{(1-2g\cos\Theta+g^2)^{3/2}}, \quad g\in[-1,1], \tag{14}$$

$$\alpha_s = (2s+1)g^s. \tag{15}$$

Note that

$$g = \langle\cos\Theta\rangle, \tag{16}$$

where

$$\langle\cos\Theta\rangle = \frac{1}{2}\int_{-1}^{+1} P(\Theta)\cos\Theta\,\mathrm{d}(\cos\Theta) = \frac{1}{3}\alpha_1 \tag{17}$$

is the asymmetry parameter of the phase function. Similarly, for the often used double-peaked Henyey–Greenstein phase function [60]

$$P(\Theta) = f\frac{1-g_1^2}{(1-2g_1\cos\Theta + g_1^2)^{3/2}} + (1-f)\frac{1-g_2^2}{(1-2g_2\cos\Theta + g_2^2)^{3/2}} \tag{18}$$

with a positive g_1 and a negative g_2, the Legendre expansion coefficients are given by

$$\alpha_s = f\alpha_{s1} + (1-f)\alpha_{s2}, \tag{19}$$

where α_{s1} and α_{s2} are given by Eq. (15) with $g = g_1$ and g_2, respectively.

The code for computing the expansion coefficients for polydisperse, homogeneous spherical particles is based on the standard Lorenz–Mie theory and the approach described in Refs. [61,62]. The code allows one to select one of the following five size distributions:

- The modified gamma distribution:

$$n(r) = \text{const} \times r^a \exp\left(-\frac{\alpha r^\gamma}{\gamma r_c^\gamma}\right). \tag{20}$$

- The log normal distribution:

$$n(r) = \text{const} \times r^{-1} \exp\left(-\frac{(\ln r - \ln r_g)^2}{2\ln^2 \sigma_g}\right). \tag{21}$$

- The power law distribution:

$$n(r) = \begin{cases} \text{const} \times r^{-3}, & r_1 \le r \le r_2, \\ 0 & \text{otherwise.} \end{cases} \tag{22}$$

- The gamma distribution:

$$n(r) = \text{const} \times r^{(1-3b)/b} \exp\left(-\frac{r}{ab}\right), \quad b \in (0, 0.5). \tag{23}$$

- The modified power law distribution:

$$n(r) = \begin{cases} \text{const}, & 0 \le r \le r_1, \\ \text{const} \times (r/r_1)^\alpha, & r_1 \le r \le r_2, \\ 0, & r_2 < r. \end{cases} \tag{24}$$

The constant for each size distribution is chosen such that the size distribution satisfies the standard normalization

$$\int_{r_{\min}}^{r_{\max}} n(r)\,\mathrm{d}r = 1. \tag{25}$$

Mathematically, particle radii in the modified gamma, log normal, and gamma distributions may extend to infinity. However, a finite $r_{\max}$ must be chosen in actual computer calculations.

There are two practical interpretations of a truncated size distribution. First, $r_{\max}$ can be increased until the scattering characteristics converge within some numerical accuracy (note that convergent $r_{\max}$ values for the modified gamma and log normal distributions can be unrealistically large for small γ or large σ_g [63]). In this case the converged truncated size distribution is numerically equivalent to the distribution with $r_{\max} = \infty$. Second, a truncated distribution can be considered a specific distribution with scattering characteristics different from those for the distribution with $r_{\max} = \infty$. Similar considerations apply to the parameter $r_{\min}$ whose mathematical value for the modified gamma, log normal, and gamma distributions is zero, but in practice can be any number smaller than $r_{\max}$. Note that for the gamma distribution with $r_{\min} = 0$ and $r_{\max} = \infty$, a and b coincide with the effective radius r_{eff} and effective variance v_{eff}, respectively, as defined by Hansen and Travis [47].

The numerical integration of scattering characteristics over a size distribution is achieved by subdividing the entire interval $[r_{\min}, r_{\max}]$ of particle radii into a number n of equal subintervals and applying a Gaussian quadrature formula with k division points to each subinterval. Note that n and/or k should be increased until the required numerical accuracy is reached.

An efficient technique for computing the Legendre expansion coefficients for polydispersions of randomly oriented, homogeneous, rotationally symmetric nonspherical particles is described in detail in Ref. [64]. This technique is based on the T-matrix approach [65] and an analytical method for averaging scattering characteristics over particle orientations [66].

The computation of the Legendre expansion coefficients for phase functions obtained with other numerical methods or measured experimentally is based on the numerical evaluation of the integral

$$\alpha_s = \frac{2s+1}{2}\int_0^{\pi} \mathrm{d}\Theta \sin\Theta P(\Theta) P_s(\cos\Theta), \tag{26}$$

which is a direct consequence of Eq. (6) and the orthogonality relation for Legendre polynomials. The integral is replaced by a Gaussian quadrature and an interpolation procedure is employed to find the phase function at Gaussian division points using the table of precomputed or measured phase function values. The Legendre polynomials are computed using the recurrence relation and the initial conditions given by Eqs. (27) and (28) below with $m = 0$. We have found that spline interpolation usually provides quite acceptable results with the exception of phase functions having very sharp features [67], such as the phase function for hexagonal ice crystals. The presence of the strong 22° and 46° halos in this latter case [68] necessitates the use of simple linear interpolation. Furthermore, the δ-function transmission peak in the ray-tracing phase function for hexagonal ice crystals must be convolved with the Fraunhofer pattern, as described in Ref. [69].

3.2. Fourier components of the phase function

The right-hand side of Eq. (5) is often written in terms of associated Legendre functions $P_s^m(x) = (-\mathrm{i})^m[(s+m)!/(s-m)!]^{1/2} P_{0m}^s(x)$, $\mathrm{i} = \sqrt{-1}$, rather than generalized spherical functions. It is well known, however, that the numerical computation of associated Legendre functions with large m and s is unstable and leads to overflows [70]. On the other hand, the computation of the generalized spherical functions via the upward recurrence relation [57,58]

$$\sqrt{(s+1)^2-m^2}P^{s+1}_{m0}(x)=(2s+1)xP^{s}_{m0}(x)-\sqrt{s^2-m^2}P^{s-1}_{m0}(x) \tag{27}$$

and initial conditions

$$P^{m-1}_{m0}(x)=0, \qquad P^{m}_{m0}(x)=(2\mathrm{i})^{-m}\sqrt{\frac{(2m)!}{m!m!}}(1-x^2)^{m/2}, \tag{28}$$

is numerically stable and efficient. Furthermore, the concept of generalized spherical functions naturally appears in the theory of polarized radiative transfer [5,58], the Lorenz–Mie theory [62], and the T-matrix method [66] and provides a natural and appealing link between these theories.

3.3. Iterative solution of the Ambartsumian's equation

By using a quadrature formula on the interval $\mu \in [0,1]$ with n division points μ_p and weights w_p, we convert integral equation (3) into a system of $n \times n$ nonlinear algebraic equations:

$$\begin{aligned}(\mu_p+\mu_q)R^m(\mu_p,\mu_q) &= \frac{\varpi}{4}P^m(-\mu_p,\mu_q)\\ &\quad+\frac{\varpi}{2}\mu_q\sum_{s=1}^{n} w_s P^m(\mu_p,\mu_s)R^m(\mu_s,\mu_q)\\ &\quad+\frac{\varpi}{2}\mu_p\sum_{s=1}^{n} w_s R^m(\mu_p,\mu_s)P^m(\mu_s,\mu_q)\\ &\quad+\varpi\mu_p\mu_q\sum_{s=1}^{n}\sum_{s'=1}^{n} w_s w_{s'} R^m(\mu_p,\mu_s)P^m(-\mu_s,\mu_{s'})R^m(\mu_{s'},\mu_q)\end{aligned} \tag{29}$$

for the unknowns $R^m(\mu_p,\mu_q)$, $p,q=1,\ldots,n$. This system is solved by simple iterations using

$$R^m_{[0]}(\mu_p,\mu_q)=\frac{\varpi}{4(\mu_p+\mu_q)}P^m(-\mu_p,\mu_q) \tag{30}$$

as the initial approximation. The iterations converge very fast for $m>0$ as well as for $m=0$ and $\varpi<0.8$. However, the convergence rate becomes very slow when $m=0$ and $1-\varpi \ll 1$.

To accelerate convergence, we use a procedure similar to those developed in Refs. [51,52] and based on the Sobolev–van de Hulst relation. Specifically, after each iteration, we compute the quantities (cf. Eq. (8))

$$\Delta_{[j]}(\mu_p)=i(-\mu_p)-2\sum_{q=1}^{n} w_q R^0_{[j]}(\mu_p,\mu_q)\mu_q i(\mu_q), \tag{31}$$

where j numbers iterations. We then improve $R^0_{[j]}(\mu_p,\mu_q)$ by replacing it with

$$R^0_{[j]}(\mu_p,\mu_q)+\kappa[\Delta_{[j]}(\mu_p)i(\mu_q)+i(\mu_p)\Delta_{[j]}(\mu_q)], \tag{32}$$

where κ is an appropriately chosen constant. This improved approximation is substituted in Eq. (31) to compute a new set of quantities $\Delta_{[j]}(\mu_p)$, which are used again to further improve $R^0_{[j]}(\mu_p, \mu_q)$ via Eq. (32), and this procedure is repeated until

$$\max_{p=1,\dots,n} |\Delta_{[j]}(\mu_p)| < 0.1\varepsilon, \tag{33}$$

where ε is the predefined absolute accuracy of computations. The improved jth iteration $R^0_{[j]}(\mu_p, \mu_q)$ is then substituted in the right-hand side of Eq. (29) to obtain the $(j+1)$th approximation $R^0_{[j+1]}(\mu_p, \mu_q)$, which is again improved using Eqs. (31) and (32), and this entire process is repeated until

$$\max_{p,q=1,\dots,n} |R^0_{[j+1]}(\mu_p, \mu_q) - R^0_{[j]}(\mu_p, \mu_q)| < \varepsilon. \tag{34}$$

de Rooij [52] suggested to use the same value $\kappa = 0.5$ in all cases. We have found, however, that this value may cause divergence when $\varpi < 0.995$ and that κ should be single-scattering-albedo specific. After having performed many numerical experiments, we have chosen the following κ values:

$$\kappa = \begin{cases} 0.5 & \text{for } \varpi \geq 0.995, \\ 0.1 & \text{for } 0.95 \leq \varpi < 0.995, \\ 0.05 & \text{for } 0.8 \leq \varpi < 0.95. \end{cases} \tag{35}$$

The use of reciprocity (Eq. (13)) reduces the number of unknowns in Eq. (29) by a factor of $2N/(N+1)$ and provides a significant saving of computer resources.

This numerical procedure renders only reflection function values $R(\mu_p,\mu_q,\varphi)$ at the division points of the quadrature formula. BRF values for μ and μ_0 not coinciding with one of the quadrature nodes must be found by numerical interpolation/extrapolation, which may result in lower accuracy than for the BRF values at the quadrature nodes. Therefore, the number of quadrature division points n should be increased until the desired numerical accuracy for all required BRF values is achieved. The accuracy can be significantly improved and n can be decreased by using the separation of the first-order scattering procedure (Section 3.7).

3.4. Computation of $i(\mu)$

Taking into account the normalization

$$\frac{1}{2}\int_{-1}^{+1} P^0(u,u')\,\mathrm{d}u' = 1, \tag{36}$$

we derive from Eqs. (9) and (10)

$$k = \frac{2(1-\varpi)}{\varpi\int_{-1}^{+1} u i(u)\,\mathrm{d}u}. \tag{37}$$

Replacing the integrals in Eqs. (9), (10), and (37) by respective quadrature sums, we obtain

$$i(\pm\mu_p) = \frac{\varpi}{2(1 \mp k\mu_p)} \sum_{q=1}^{n} w_q[i(\mu_q)P^0(\pm\mu_p, \mu_q) + i(-\mu_q)P^0(\pm\mu_p, -\mu_q)], \tag{38}$$

$$\frac{\varpi}{2} \sum_{p=1}^{n} w_p[i(\mu_p) + i(-\mu_p)] = 1, \tag{39}$$

$$k = \frac{2(1-\varpi)}{\varpi\sum_{p=1}^{n} w_p\mu_p[i(\mu_p) - i(-\mu_p)]}. \tag{40}$$

Substituting $k = \sqrt{1-\varpi}$, $i(\mu_p) = 2$, and $i(-\mu_p) = 1/2$ as the initial approximation, we calculate the right-hand side of Eq. (38) to obtain the next approximation for $i(\mu_p)$ and $i(-\mu_p)$. Since this approximation may not satisfy the normalization of Eq. (39), we improve $i(\mu_p)$ and $i(-\mu_p)$ by dividing them by

$$\frac{\varpi}{2} \sum_{p=1}^{n} w_p[i(\mu_p) + i(-\mu_p)]. \tag{41}$$

This improved approximation satisfies Eq. (39) and is used to compute the next approximation for k via Eq. (40). The new k, $i(\mu_p)$, and $i(-\mu_p)$ values are substituted in the right-hand side of Eq. (38) to obtain the next approximation for $i(\mu_p)$ and $i(-\mu_p)$, and so on. The process is continued until $i(\mu_p)$ and $i(-\mu_p)$ converge within 0.1ε. Note that this scheme is different from that described in Ref. [51]. Dlugach and Yanovitskij [51] compute $i(\pm\mu)$ using the expansion coefficients α^s and a method of continued fractions. We have found, however, that the use of the expansion coefficients of the original phase function to compute $i(\pm\mu)$ conflicts with the use of the renormalized phase function (Section 3.6 below) in Eq. (29) and may lead to divergence of the iterative solution of Eq. (29) for highly anisotropic phase functions. Our new procedure for computing $i(\pm\mu)$ uses the already renormalized phase function and produces numerically stable and convergent results.

3.5. Numerical integration

The Gauss quadrature formula (e.g., Ref. [71]) has the highest algebraic degree of precision (i.e., a formula with n nodes is exact for all polynomials of degree $2n-1$ and lower) and is traditionally used in radiative transfer calculations to numerically evaluate integrals on the interval [0,1] (e.g., Refs. [72–74]). A significant disadvantage of this quadrature is that the largest node is always smaller than 1, and if BRF values for normal incidence and/or reflection are required, then one must use an extrapolation procedure. Unfortunately, extrapolation often produces poor numerical accuracy (e.g., see discussion on pp. 210 and 211 of Ref. [52]) and necessitates the use of the Gaussian quadrature formula with a large number of nodes. We have found that a more efficient approach is to use the so-called Markov quadrature formula (Chapter 9.2 of Ref. [71]) with one predefined node at $\mu = 1$. This formula still has the highest possible algebraic precision and is exact for all polynomials of degree $2n-2$ and lower. Furthermore, it allows one to avoid the use of the extrapolation procedure or the so-called extra points (Ref. [47] and L.D. Travis, personal communication). Multiple numerical tests have shown that the Gaussian and Markov quadratures

Table 1
Division points and weights of the Markov quadrature formula on the interval [0,1] with $n = 30$

	μ	w
1	0.00160587785254	0.00411899413797
2	0.00844194880403	0.00954444032329
3	0.02066193363616	0.01487343889309
4	0.03813469699711	0.02004018939073
5	0.06066914207658	0.02498751843953
6	0.08801845813989	0.02966112217483
7	0.11988302768490	0.03400976899322
8	0.15591374708438	0.03798580509944
9	0.19571586157012	0.04154566451353
10	0.23885329363337	0.04465034297146
11	0.28485342210352	0.04726582410455
12	0.33321226086401	0.04936345167913
13	0.38339998090611	0.05092024336491
14	0.43486671538603	0.05191914244132
15	0.48704858415304	0.05234920462588
16	0.53937387177272	0.05220571795295
17	0.59126929137078	0.05149025437772
18	0.64216626567319	0.05021065253237
19	0.69150715642309	0.04838093181641
20	0.73875137391194	0.04602113875159
21	0.78338129966059	0.04315712726339
22	0.82490795730055	0.03982027524838
23	0.86287636938624	0.03604714041164
24	0.89687054110030	0.03187905880664
25	0.92651801527194	0.02736168939988
26	0.95149394561648	0.02254450560005
27	0.97152463085599	0.01748022010489
28	0.98639040253929	0.01222402012888
29	0.99592721636071	0.00683100534121
30	1.00000000000000	0.00111111111111

with a number of nodes n larger than about 10 have essentially the same numerical accuracy for intermediate μ and μ_0 values, whereas the Markov quadrature produces much better accuracy for μ and/or μ_0 equal to 1. Since the CPU time consumption in solving Eq. (29) is proportional to n^3, the use of the Markov quadrature with a reduced number of nodes results in a significant saving of computer resources. We have developed a simple, efficient, and highly accurate FORTRAN procedure for computing the nodes and weights of the Markov quadrature formula with an arbitrary n. Table 1exemplifies the performance of the procedure and lists the nodes and weights of the Markov quadrature with $n = 30$.

The direct application of a quadrature formula to the integration μ-interval [0,1] is a standard approach in the radiative transfer theory (e.g., Refs. [47–49,51,55,61,72–74]). However, it provides poor sampling of zenith angles close to 0° and, as multiple numerical tests have shown, causes a very slow convergence of $R^0(1,1)$ with increasing n for particles large compared to the wavelength. This happens even when the Markov quadrature is used and no extrapolation is involved or when the Gaussian quadrature is used along with an extra point at $\mu = \mu_0 = 1$. On the other hand, convergence with increasing n is fast for $\mu < 1$ and $\mu_0 < 1$. We have found that a very efficient way of avoiding excessive n values in radiative transfer computations is to apply the Gaussian quadrature to the interval $[0, \pi/2]$ of zenith angle values. Since

$$\int_0^1 f(\mu)\,\mathrm{d}\mu = \int_0^{\pi/2} f(\cos\vartheta)\sin\vartheta\,\mathrm{d}\vartheta, \tag{42}$$

we easily derive the following expressions for the respective division points and weights in Eq. (29):

$$\mu_p = \cos\left(\frac{\pi}{4}X_p + \frac{\pi}{4}\right), \qquad w_p = W_p \sin\left(\frac{\pi}{4}X_p + \frac{\pi}{4}\right), \quad p = 1, \dots, n, \tag{43}$$

where X_p and W_p are Gaussian nodes and weights, respectively, on the interval $[-1, +1]$. These division points provide a much better sampling of zenith angles close to 0° and a much higher convergence rate for $R^0(1,1)$ with increasing n than the Gaussian or the Markov quadrature formula applied to the interval $[0,1]$ of μ values.

3.6. Renormalization of the phase function

Although analytically the zeroth Fourier component of the phase function must be normalized according to Eq. (36), the numerical evaluation of the left-hand side of Eq. (36) usually produces μ-dependent numbers not equal to 1:

$$\frac{1}{2}\sum_{q=1}^{n} w_q[P^0(\mu_p, \mu_q) + P^0(\mu_p, -\mu_q)] = \delta_p \neq 1. \tag{44}$$

This results in a deviation of the "numerical" single-scattering albedo from its actual value and, for nonabsorbing or weakly absorbing media, can lead to an efficient "photon gain"or "photon loss". A direct adverse consequence is a serious violation of energy conservation and poor numerical accuracy. Hansen [55] developed a so-called renormalization procedure, which numerically enforces the normalization of Eq. (36) by slightly modifying the $P^0(\mu_p, \mu_q)$ values. We have found that the renormalization procedure of Ref. [55] produces accurate BRFs in most cases, but not always. Therefore, we have developed an alternative renormalization procedure, which is simpler than that of Ref. [55] and appears to be more stable. Specifically, we multiply the quantities $P^0(\mu_p, \mu_p)$, $p = 1, \dots, n$ by the correction factors

$$\varepsilon_p = 1 + \frac{2 - 2\delta_p}{w_p P^0(\mu_p, \mu_p)}, \quad p = 1, \dots, n. \tag{45}$$

This correction makes the left-hand side of Eq. (44) equal to 1 for any p and is applied to higher Fourier components of the phase function as well. Since it affects only the forward-scattering values of the phase function, it has negligible effect on the bidirectional reflection function while numerically ensuring energy conservation.

3.7. Separation of the first-order-scattering contribution to the reflection function

For large scattering particles with highly variable phase functions and for μ and μ_0 significantly smaller than 1, one may need very many Fourier terms in Eq. (2) in order to accurately represent the reflection function. On the other hand, it is also known that with μ and μ_0 approaching zero the only significant contribution to the reflection function comes from photons scattered only once [56]. This suggests the idea of subtracting the first-order-scattering contribution from all Fourier components of the reflection function, thereby greatly reducing the number of numerically significant Fourier components, evaluating the right-hand side of Eq. (2), interpolating (if necessary) this slowly varying high-order-scattering part of the reflection function, and finally adding the exact single-scattering contribution [75]. The latter contribution can be easily computed analytically for the scattering angle Θ corresponding to a specific combination of μ, μ_0, and φ values and given by

$$\cos\Theta = -\mu\mu_0 + \sqrt{1-\mu^2}\sqrt{1-\mu_0^2}\cos\varphi. \tag{46}$$

In other words, the total reflection function is represented in the form

$$R(\mu,\mu_0,\varphi) = R_1(\mu,\mu_0,\varphi) + \sum_{m=0}^{m_1}(2-\delta_{m0})[R^m(\mu,\mu_0) - R_1^m(\mu,\mu_0)]\cos m\varphi, \tag{47}$$

where $\delta_{mm'}$ is the Kronecker delta,

$$R_1(\mu,\mu_0,\varphi) = \frac{\varpi}{4(\mu+\mu_0)}P(\Theta), \tag{48}$$

$$R_1^m(\mu,\mu_0) = \frac{\varpi}{4(\mu+\mu_0)}P^m(-\mu,\mu_0) \tag{49}$$

and $m_1 \ll m_{\max}$ [48]. The term in square brackets on the right-hand side of Eq. (47) is a smooth function of μ and μ_0 and can be accurately interpolated even when the number of quadrature nodes is relatively small, while $P(\Theta)$ is computed via Eqs. (6) and (46).

4. Computations and discussion

4.1. Soil surfaces

Table 2 lists parameters of four soil particle models used in the computations described below. We assume the standard gamma size distribution of Eq. (23) with an effective radius of $a = r_{\text{eff}} = 10$ μm and an effective variance of $b = v_{\text{eff}} = 0.1$. This effective radius is typical of soil particles (e.g., Ref. [76]). The four values of the refractive index $m = m_r + im_i$ are also typical of soil particles at the visible wavelength $\lambda = 0.63$ μm considered [76]. The single scattering properties of the four soil particle models were computed assuming the spherical particle shape and using the Lorenz–Mie theory. (It should be noted, however, that the Lorenz–Mie theory does not necessarily provide the best representation of soil particle phase functions [77–80]). Table 2 gives the

Table 2
Soil particle models

Model	a (μm)	b	m_r	m_i	ϖ	$\langle\cos\Theta\rangle$	$s_{\max}$	A_S	A_S(HG)	A_S(HH)
1	10	0.1	1.55	0.001	0.85404	0.83752	641	0.1399	0.1382	0.1655
2	10	0.1	1.55	0.002	0.76137	0.86568	644	0.0727	0.0716	0.0889
3	10	0.1	1.55	0.003	0.69923	0.88582	645	0.0472	0.0464	0.0588
4	10	0.1	1.55	0.004	0.65646	0.90054	646	0.0345	0.0339	0.0435

respective values of the single-scattering albedo ϖ, asymmetry parameter of the phase function $\langle\cos\Theta\rangle$, the number of terms in the Legendre decomposition of the phase function $s_{\max}$ (Eq. (6)), and the spherical albedo A_S. Note the significant decrease of ϖ and increase of $\langle\cos\Theta\rangle$ with increasing imaginary part of the refractive index. The solid curves in the upper panel of Fig. 2 show the respective Lorenz–Mie phase functions, while the dotted curves show the asymmetry-parameter-equivalent Henyey–Greenstein phase functions (Eq. (14)).

Table 2 also gives spherical albedo values computed using the equivalent Henyey–Greenstein phase function, A_S(HG), and the simple approximate formula

$$A_S(\mathrm{HH}) = (1 - s)/(1 + s) \tag{50}$$

derived by Hovenier and Hage [81], where

$$s = \sqrt{\frac{1 - \varpi}{1 - \varpi\langle\cos\Theta\rangle}} \tag{51}$$

is the so-called similarity parameter [56]. It is seen that the A_S(HG) values are quite close to the exact ones, while the Hovenier and Hage approximation provides somewhat lower accuracy.

Solid curves in the upper panel of Fig. 3 depict the plane albedo A_P as a function of the cosine of the illumination zenith angle μ_0. Note that A_P is determined only by the 0th component of the reflection function via Eq. (11) and, as a consequence, the computation of the upper panel of Fig. 3 using 50 quadrature division points took less than 2 s of CPU time on an IBM RISC model 397 workstation. We also computed the plane albedo using the asymmetry-parameter-equivalent Henyey–Greenstein phase functions and the δ-Eddington approximation [82]. The ratios of these approximate plane albedo values relative to the exact ones are shown by the dotted and solid curves, respectively, in the bottom panel of Fig. 3. Not surprisingly, plane albedos decrease with increasing the imaginary part of the refractive index and, thus, decreasing the single-scattering albedo. Both the δ-Eddington approximation and the asymmetry-parameter-equivalent Henyey–Greenstein phase function produce significant errors, especially for grazing illumination. Using the asymmetry-parameter-equivalent Henyey–Greenstein phase function overestimates the plane albedo for small μ_0 and underestimates it for μ_0 close to 1, which is naturally explained by the scattering-angle pattern of the phase function differences (upper panel of Fig. 2). The errors increase significantly with increasing absorption. This can be explained by the increasing contribution of photons scattered only once and by the large differences in the single-scattering phase functions.

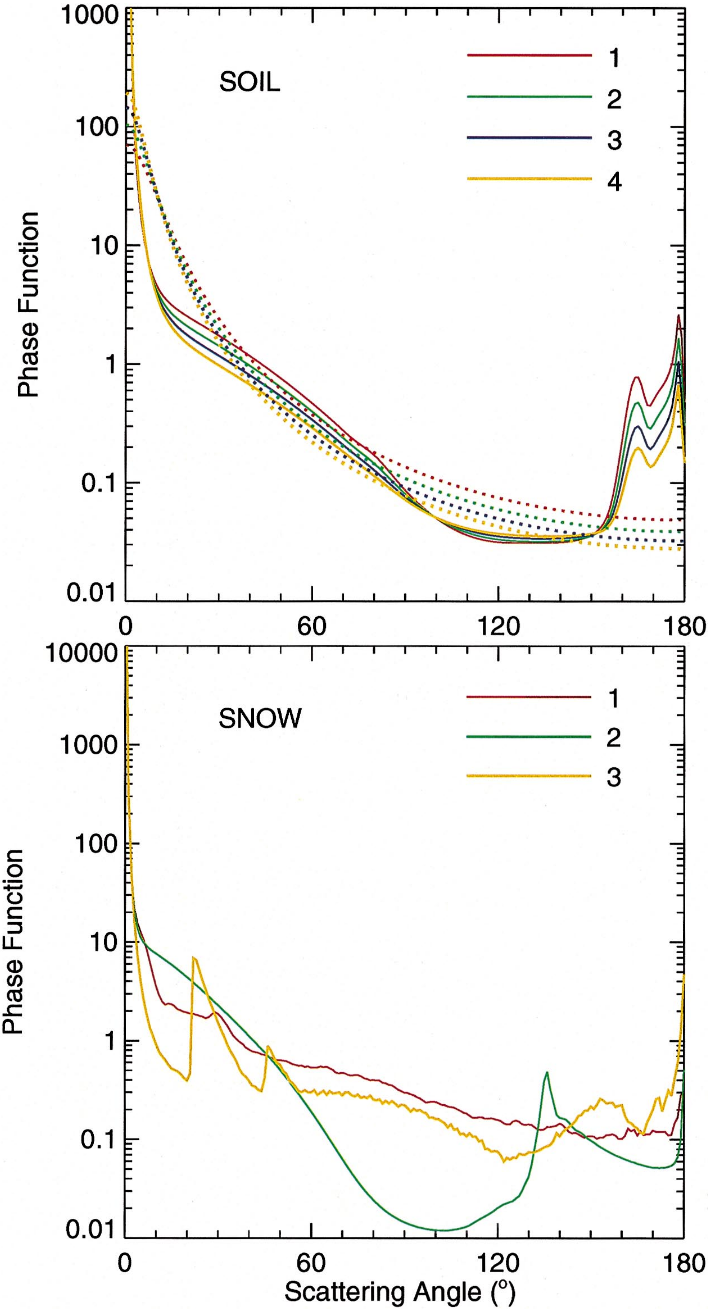

Fig. 2. Phase functions for soil particle models 1–4 (upper panel) and snow particle models 1–3. Dotted curves in the upper panel show asymmetry-parameter-equivalent Henyey–Greenstein phase functions.

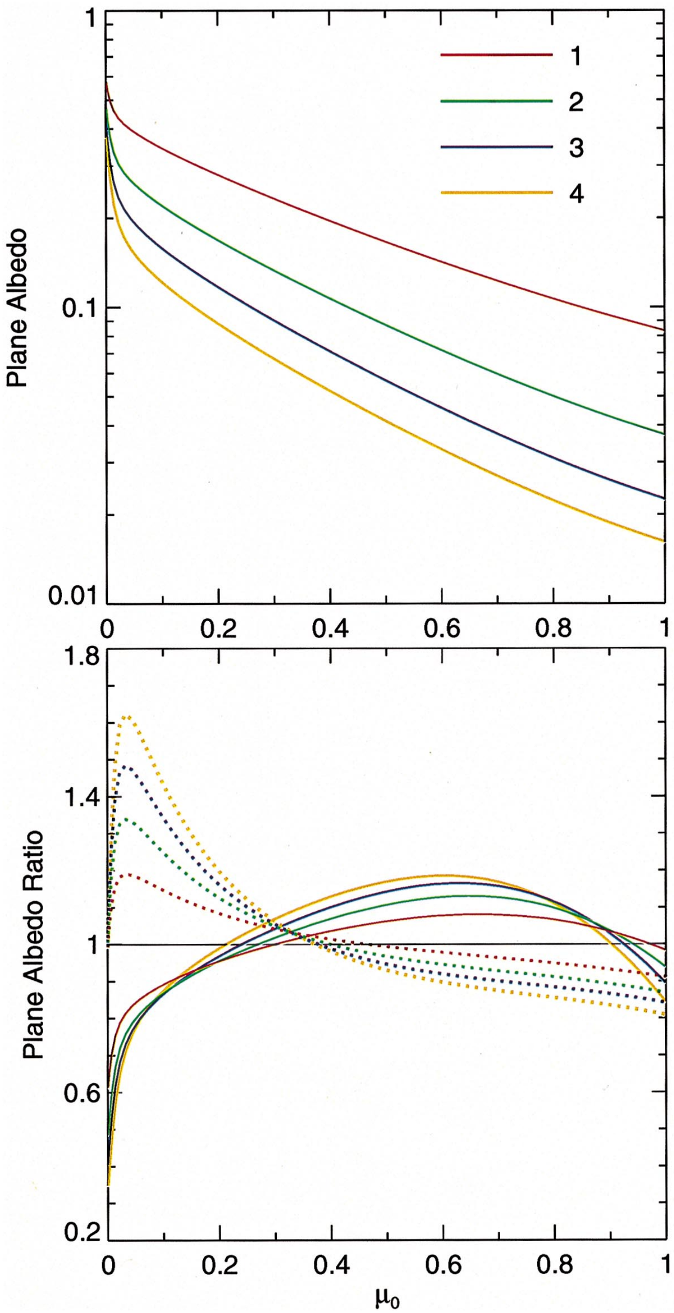

Fig. 3. Upper panel: plane albedo versus μ_0 for soil particle models 1–4. Lower panel: plane albedos computed using the δ-Eddington approximation (solid curves) and asymmetry-parameter-equivalent Henyey–Greenstein phase functions (dotted curves) relative to the exact values for soil particle models 1–4.

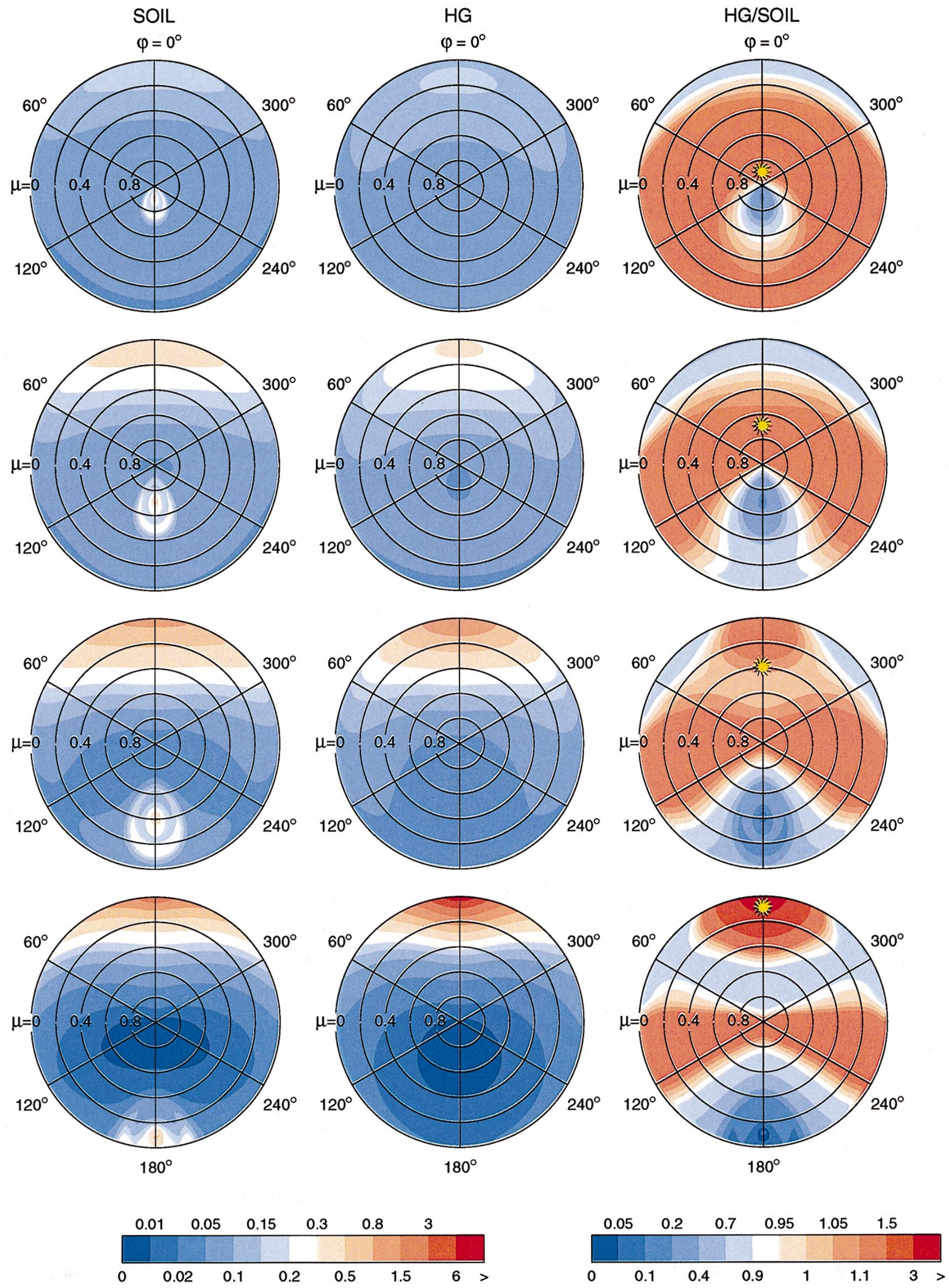

Fig. 4. Left column: reflected intensity versus μ and φ for soil particle model 1. Middle column: the same but for the asymmetry-parameter-equivalent Henyey–Greenstein phase function. Right column: the ratio of the intensities shown in the middle and left columns. The four values of the cosine of the illumination zenith angle $\mu_0 = 0.9$, 0.7, 0.4, and 0.1 are indicated by the yellow stars in the right column. The azimuth angle of the incident radiation is zero.

The much better accuracy of the A_S(HG) values in Table 2 can be explained by cancellation of the plane albedo errors after integrating over μ_0 in Eq. (12).

Fig. 4 shows the angular distribution of the reflected intensity computed for soil particle model 1 using the exact Lorenz–Mie phase function and its Henyey–Greenstein counterpart and assuming $F = 1$ in Eq. (1). The computations for the exact phase function used 100 quadrature nodes and took about 25 min of CPU time including the Lorenz–Mie computation of the Legendre expansion coefficients, the solution of Eq. (3), and interpolation. The computations for the equivalent Henyey–Greenstein phase function used 50 quadrature nodes and took less than 3 min.

Two obvious features of the reflected intensity distributions shown in the left column are the backscattering enhancement ($\mu = \mu_0$, $\varphi = 180°$) caused by the glory in the Lorenz–Mie phase function (upper panel of Fig. 2) and the strong near-forward scattering for the cases of grazing and near-grazing incidence caused by the phase function peak at small scattering angles. The reflectance patterns for the equivalent Henyey–Greenstein phase function exhibit only the second feature, which is explained by the absence of the backscattering phase function peak similar to the glory. The right column of Fig. 4 shows that BRF errors caused by the use of the equivalent Henyey–Greenstein phase function can be very large and can exceed a factor of 20 at backscattering geometries and a factor of 3 at near-forward-scattering geometries. These errors can be unequivocally attributed to the phase function differences. Thus, Fig. 4 makes a strong case against using approximate phase functions in BRF computations for semi-infinite particulate media.

4.2. Snow surfaces

In this section we describe BRF computations for three snow particle models summarized in Table 3.The assumed wavelength is $\lambda = 0.65$ µm. Model 1 particles have highly irregular, random-fractal shapes introduced in Ref. [83]; model 2 particles are homogeneous ice spheres; and model 3 particles are regular hexagonal ice crystals with a length-to-diameter ratio of 2. The nonspherical model 1 and 3 particles are randomly oriented in three-dimensional space. For all three models we used the same power law distribution of radii or projected-area-equivalent-sphere radii (Eq. (22)) with an effective radius of 50 µm and an effective variance of 0.2. The respective phase functions were computed using the ray-tracing technique [83] coupled with the Kirchhoff approximation [69] for models 1 and 3 and the Lorenz–Mie theory for model 2. They are shown in the lower panel of Fig. 2 and exhibit large differences exceeding an order of magnitude at some scattering angles. The resulting differences in the asymmetry parameter are also significant (Table 3). As discussed in Ref. [84], the phase functions of models 1 and 3 may represent limiting cases of highly distorted and

Table 3
Snow particle models

Model	Shape	r_{eff} (µm)	v_{eff}	m_r	m_i	ϖ	$\langle\cos\Theta\rangle$	$s_{\max}$
1	Irregular	50	0.2	1.311	0	1	0.7524	2000
2	Spherical	50	0.2	1.311	0	1	0.8860	1948
3	Hexagonal	50	0.2	1.311	0	1	0.8117	2000

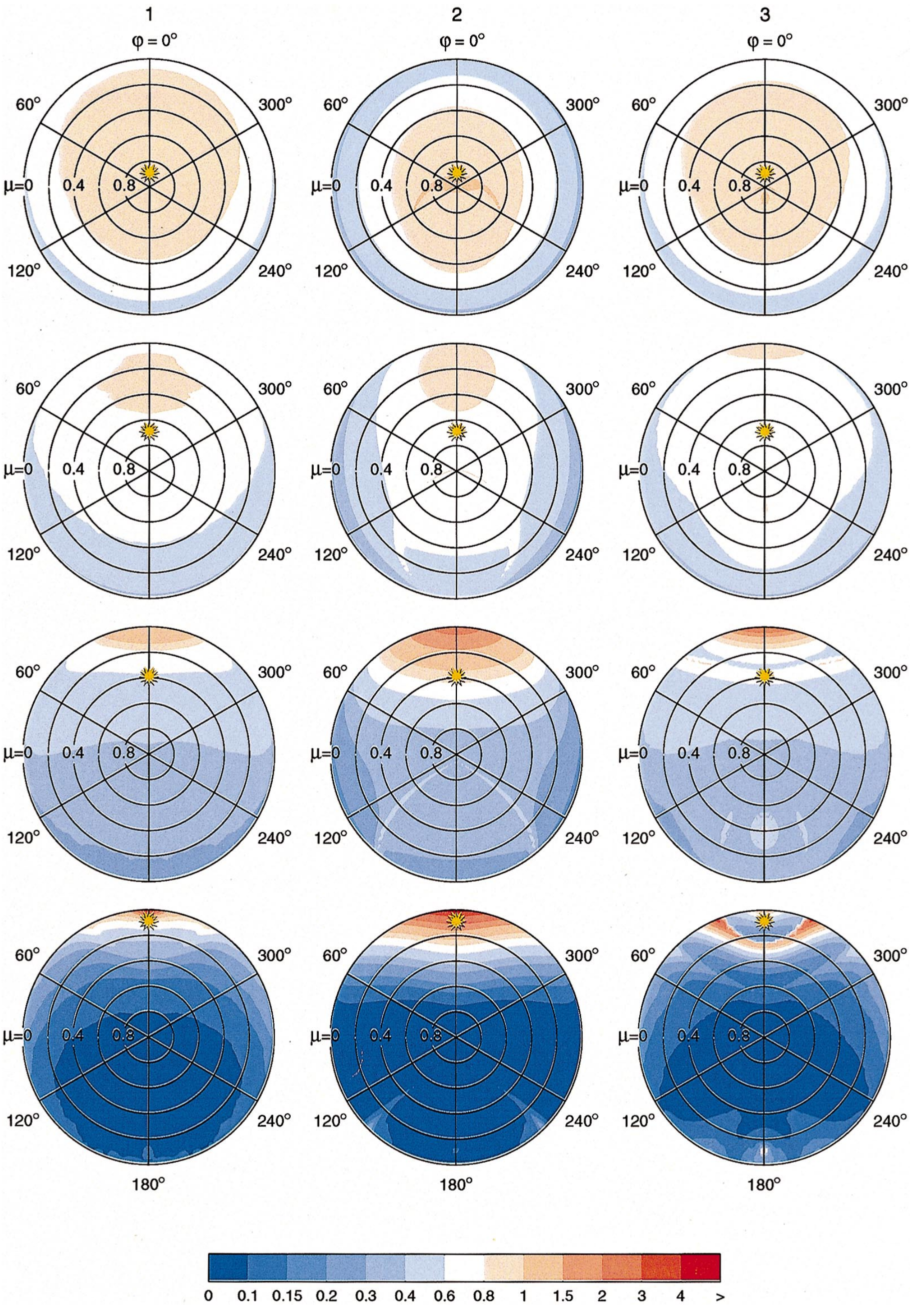

Fig. 5. Reflected intensity versus μ and φ for snow particle models 1, 2, and 3. The four values of the cosine of the illumination zenith angle $\mu_0 = 0.9$, 0.7, 0.4, and 0.1 are indicated by the yellow stars. The azimuth angle of the incident radiation is zero.

pristine ice crystals, respectively. Since water ice is essentially nonabsorbing at visible wavelengths, the single-scattering, plane, and spherical albedos for all three models are equal to unity.

Fig. 5 shows the reflected intensities for the three snow particle models, while Fig. 6 depicts the ratios 2/1, 3/1, and 3/2 of intensities for the respective models. It is obvious that the shape of the

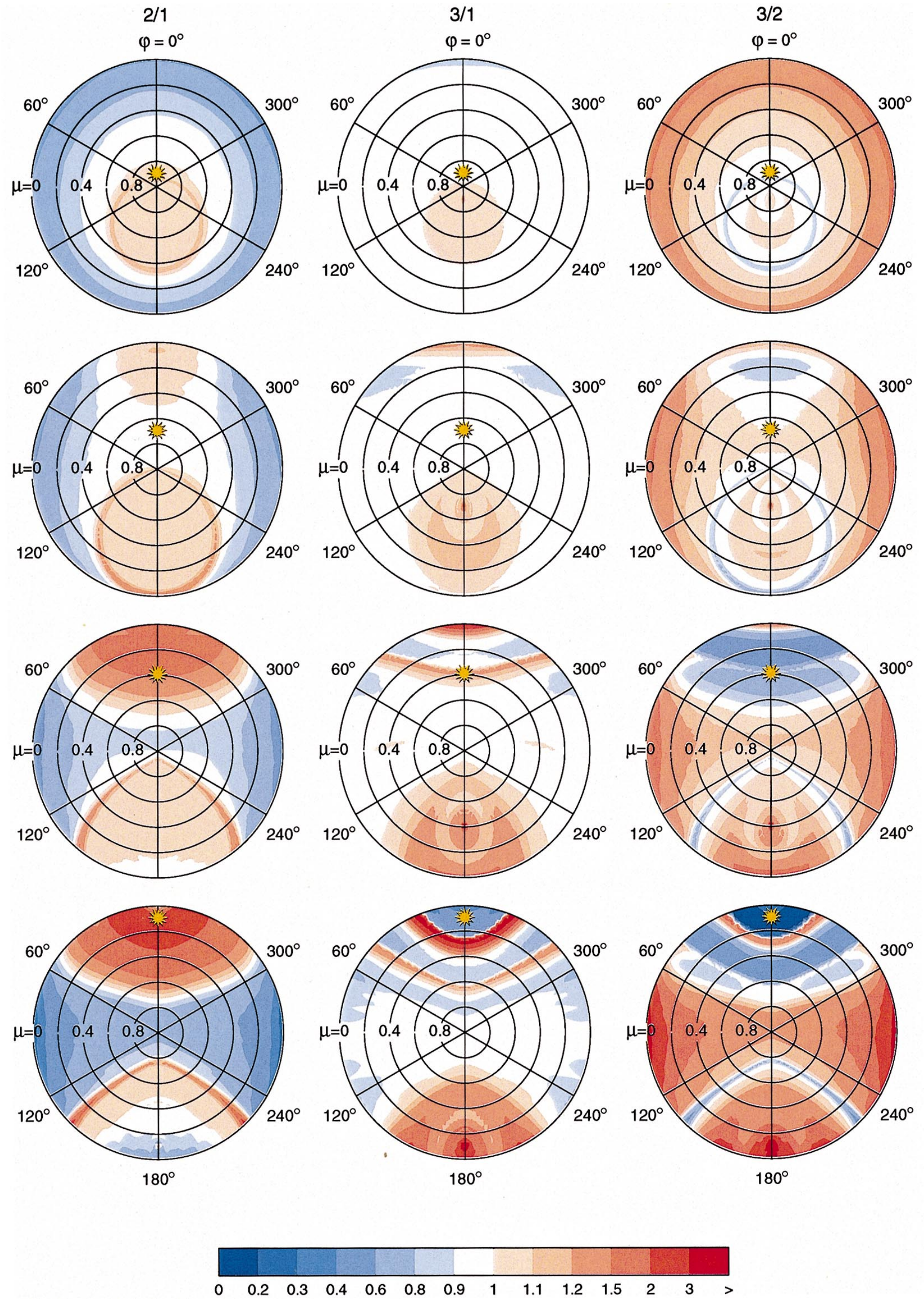

Fig. 6. As in Fig. 4, but for ratios of reflected intensities.

scattering particles has a profound effect on the reflectance of flat snow surfaces. Although radiance differences between the different models are relatively small at nearly normal incidence ($\mu_0 = 0.9$), they significantly increase with decreasing μ_0 and result in intensity ratios smaller than 0.2 and larger than 3 (cf. Ref. [84]). This is a direct consequence of the increasing relative contribution of the first-order scattering to the reflection function and the large phase function differences. Hexagonal snow crystals (model 3) produce the most structured radiance field dominated by the backscattering peak and the primary (22°) and secondary (46°) halos (two lower panels in the right column of Fig. 5). These features clearly show up in the 3/1 and 3/2 intensity ratios (Fig. 6). The spherical ice particles produce a noticeable enhancement of intensity caused by the rainbow. This feature is especially well seen in the 2/1 ratio. The radiance field produced by the featureless phase function of irregular snow crystals (model 1) is by far the least structured (left column of Fig. 5). These results emphasize the importance of accurate treatment of single-scattering phase functions for realistic snow grain models.

5. Conclusions

We have described in detail an efficient technique for computing bidirectional reflectance of semi-infinite discrete random media based on an exact numerical solution of the radiative transfer equation. This technique results in a very compact and fast computer code and produces BRFs which fully comply with reciprocity and energy conservation. The high efficiency and accuracy of the technique make far less tempting the use of approximations such as the δ-Eddington approximation, the asymmetry-parameter-equivalent Henyey–Greenstein phase function, and the truncation of the phase function [73] and provide an ideal tool for testing the accuracy of approximate approaches [81,85]. Our sample computations for flat soil and snow surfaces have clearly demonstrated the limited applicability of approximate treatments of the single-scattering phase function in BRF modeling.

Since we considered only nonabsorbing or weakly absorbing media, we ignored the opposition effect caused by the so-called shadow hiding [1]. Other factors ignored in the model are the effects of polarization [53–55], packing density [35,41,86–91], and coherent backscattering [29,30,32,38, 43,92]. However, they can be incorporated in a rather straightforward manner, as described, e.g., in Refs. [26–28,52,93–95]. This is the subject of our current research. An equally challenging problem of macroscopic surface roughness [8,12,19,24,46,96] can be addressed by convolving BRFs computed as described in this paper with a Monte Carlo procedure handling multiple surface reflections and surface shadowing. As pointed out in the introduction, this approach avoids time-consuming ray tracing inside a nonabsorbing or weakly absorbing, optically semi-infinite medium and provides a great saving of computer resources. The ultimate challenge is to take into account the effects of the discontinuous nature of light scattering in densely packed discrete random media [31,35,97], but this requires the development of a much more sophisticated approach.

Acknowledgements

We thank Brian Cairns, Joop Hovenier, and Andrew Lacis for careful reading of the manuscript and useful comments and Lilly Del Valle for help with graphics. This research was sponsored by the NASA Radiation Science Program and NASA Global Aerosol Climatology Project managed by Dr. Robert Curran.

References

[1] Bowell E, Hapke B, Domingue D, Lumme K, Peltoniemi J, Harris AW. Application of photometric models to asteroids. In: Binzel RP, Gehrels T, Matthews MS, editors. Asteroids II. Tucson, AZ, USA: Arizona Univ. Press, 1989. p. 524–56; Buratti BJ, Hillier JK, Wang M. Icarus 1996;124:490–9; Goguen JD. Icarus 1999, submitted for publication; Helfenstein P, Currier N, Vlark BE et al. Icarus 1998;135:41–63; Verbiscer A, Helfenstein P. Reflectance spectroscopy of icy surfaces. In: Schmitt B et al., editors. Solar System Ices. Dordrecht: Kluwer, 1998. p. 157–97.

[2] Brandt RE, Grenfell TC, Warren SG. Antarctic J US 1991;26:272–5.

[3] Bréon F-M, Tanré D, Lecomte P, Herman M. IEEE Trans Geosci Remote Sens 1995;33:487–99.

[4] Deering DW, Eck TF, Otterman J. Agric Forest Meteorol 1990;52:71–93.

[5] de Haan JF. Effects of aerosols on the brightness and polarization of cloudless planetary atmospheres. Ph.D. thesis, Free University, Amsterdam, 1987.

[6] den Outer P. Multiple light scattering in random discrete media: Coherent backscattering and imaging. Ph.D. thesis, University of Amsterdam, 1995.

[7] Douté S, Schmitt B. J Geophys Res 1998;103:31367–89.

[8] Dozier J. Remote sensing of snow in the visible and near-infrared wavelengths. In: Asrar G, editor. Theory and applications of optical remote sensing. New York: Wiley, 1989. p. 527–47.

[9] Fily M, Bourdells B, Dedieu JP, Sergent C. Remote Sens Environ 1997;59:452–60; Fily M, Leroux C, Lenoble J, Sergent C. Terrestrial snow studies from remote sensing in the solar spectrum and the thermal infrared. In: Schmitt B et al. editors. Solar system ices. Dordrecht: Kluwer, 1998. p. 421–41.

[10] Jin Z, Simpson JJ. IEEE Trans Geosci Remote Sens 1999;37:543–54.

[11] Gibbs DP, Betty CL, Fung AK, Blanchard AJ, Irons JR, Balsam WL. Remote Sens Environ 1993;43:97–114.

[12] Grenfell TC, Warren SG, Mullen PC. J Geophys Res 1994;99:18669–84.

[13] Hapke B. Theory of reflectance and emittance spectroscopy. New York: Cambridge Univ. Press, 1993.

[14] Hendricks TJ, Howell JR. ASME J Heat Transfer 1996;118:79–87.

[15] Irons JR, Weismiller RA, Petersen GW. Soil reflectance. In: Asrar G, editor. Theory and applications of optical remote sensing. New York: Wiley, p. 66–106.

[16] Irons JR, Campbell GS, Norman JM, Graham DW, Kovalick WM. IEEE Trans Geosci Remote Sens 1992;30:249–60.

[17] Jafolla JC, Stokes JA, Sullivan RJ. Proc SPIE 1997;3141:1–12.

[18] Kuhn M. Ann Glaciol 1985;6:164–7.

[19] Leroux C, Fily M. J Geophys Res 1998;103:25779–88.

[20] Leroux C, Deuzé J-L, Goloub P, Sergent C, Fily M. J Geophys Res 1998;103:19721–31.

[21] Leroux C, Lenoble J, Brogniez G, Hovenier JW, de Haan JF. JQSRT 1999;61:273–85.

[22] Li S. A model for the anisotropic reflectance of pure snow. Ph.D. thesis, University of California at Santa Barbara, USA, 1982.

[23] Liang S, Mishchenko MI. Remote Sens Environ 1997;60:163–73.

[24] Lumme K, Peltoniemi JI, Irvine WM. Transp Theory Statist Phys 1990;19:317–32.

[25] Martonchik JV, Diner DJ, Pinty B, Verstraete MM, Myneni RB, Knyazikhin Yu, Gordon HR. IEEE Trans Geosci Remote Sens 1998;36:1266–81.

[26] Mishchenko MI. Astrophys Space Sci 1992;194:327–33.

[27] Mishchenko MI. Astrophys J 1993;411:351–61.

[28] Mishchenko MI. JQSRT 1994;52:95–110.

[29] Mishchenko MI, Dlugach JM. Mon Not Roy Astron Soc 1992;254:15–18.

[30] Mishchenko MI, Dlugach JM. Planet Space Sci 1993;41:173–81.

[31] Mishchenko MI, Macke A. JQSRT 1997;57:767–94.

[32] Muinonen K. Coherent backscattering by solar system dust particles. In: Milani A et al., editors. Asteroids, comets, meteors. Dordrecht: Kluwer, 1993. p. 271–96.
[33] Nelson HF, Look DC, Crosbie AL. ASME J Heat Transfer 1986;108:619–25.
[34] Nolin AW, Dozier J. Remote Sens Environ 1993;44:231–8.
[35] Peltoniemi JI, Lumme K. J Opt Soc Am A 1992;9:1320–6.
[36] Pinty B, Verstraete MM. Remote Sens Environ 1992;41:155–67.
[37] Pitter MC, Jakeman E, Harris M. J Mod Opt 1998;45:1557–65.
[38] POAN Research Group, editor. New aspects of electromagnetic and acoustic wave diffusion. Berlin: Springer, 1998.
[39] Steffen K. Effect of solar zenith angle on snow anisotropic reflectance. In: Smith WL, Stamnes K, editors. IRS'96: current problems in atmospheric radiation. VA, USA: Deepak Publ., Hampton, 1997. p. 41–4.
[40] Taylor VR, Stowe L. J Geophys Res 1984;89:4987–96.
[41] Tien CL. ASME J Heat Transfer 1988;110:1230–42.
[42] van Der Mark MB. Propagation of light in disordered media: a search for Anderson Localization. Ph.D. thesis, University of Amsterdam, 1990.
[43] van Tiggelen BA. Multiple scattering and localization of light. Ph.D. thesis, University of Amsterdam, 1992.
[44] Tsay S-C, King MD, Arnold GT, Li JY. J Geophys Res 1998;103:31,943–53; Soulen PF, Tsay S-C, King MD, Arnold GT, Jason YL. J Geophys Res 1999, in press.
[45] Warren SG. Rev Geophys 1982;20:67–89.
[46] Warren SG, Brandt RE, Hinton PO'R. J Geophys Res 1998;103:25789–807.
[47] Hansen JE, Travis LD. Space Sci Rev 1974;16:527–610.
[48] de Haan JF, Bosma PB, Hovenier JW. Astron Astrophys 1987;183:371–91.
[49] Stamnes K. Rev Geophys 1986;24:299–310.
[50] Sobolev VV. Light scattering in planetary atmospheres. Oxford: Pergamon Press, 1975 [chapter 2].
[51] Dlugach JM, Yanovitskij EG. Icarus 1974;22:66–81; Yanovitskij EG. Light scattering in inhomogeneous atmospheres. Berlin: Springer, 1997 [chapters 2 and 3].
[52] de Rooij WA. Reflection and transmission of polarized light by planetary atmospheres. Ph.D. thesis, Free University, Amsterdam, 1985.
[53] Mishchenko MI, Lacis AA, Travis LD. JQSRT 1994;51:491–510.
[54] Lacis AA, Chowdhary J, Mishchenko MI, Cairns B. Geophys Res Lett 1998;25:135–8.
[55] Hansen JE. J Atmos Sci 1971;28:1400–28.
[56] van de Hulst HC. Multiple light scattering. New York: Academic Press, 1980.
[57] Gelfand IM, Minlos RA, Shapiro ZYa. Representations of the rotation and Lorentz groups and their applications. Oxford: Pergamon Press, 1963.
[58] Hovenier JW, van der Mee CVM. Astron Astrophys 1983;128:1–16.
[59] de Rooij WA, Domke H. JQSRT 1984;31:285–99.
[60] Irvine WM. Astrophys J 1965;142:1563–75.
[61] King MD. JQSRT 1983;30:143–61.
[62] de Rooij WA, van der Stap CCAH. Astron Astrophys 1984;131:237–48.
[63] Lacis AA, Mishchenko MI. Climate forcing, climate sensitivity, and climate response: a radiative modeling perspective on atmospheric aerosols. In: Charlson RJ, Heintzenberg J, editors. Aerosol Forcing of Climate. New York: Wiley, 1995. p. 11–42.
[64] Mishchenko MI, Travis LD. JQSRT 1998;60:309–24.
[65] Mishchenko MI, Travis LD, Mackowski DW. JQSRT 1996;55:535–75.
[66] Mishchenko MI. J Opt Soc Am A 1991;8:871–82.
[67] Muinonen K, Lumme K, Peltoniemi J, Irvine WM. Appl Opt 1989;28:3051–60.
[68] Takano Y, Liou KN. J Atmos Sci 1989;46:3–19.
[69] Mishchenko MI, Macke A. J Geophys Res 1998;103:1799–805.
[70] Dave JV, Armstrong BH. JQSRT 1970;10:557–62.
[71] Krylov VI. Approximate calculation of integrals. New York: Macmillan, 1962.
[72] Adams CN, Kattawar GW. JQSRT 1970;10:341–56.

[73] Lenoble J, editor. Radiative transfer in scattering and absorbing atmospheres: standard computational procedures. Hampton, VA, USA: Deepak, 1985.
[74] Nakajima T, King MD. Appl Opt 1992;31:7669–83.
[75] Hansen JE, Pollack JB. J Atmos Sci 1970;27:265–81.
[76] Ishida T, Ando H, Fukuhara M. Remote Sens Environ 1991;38:173–82.
[77] Jaggard DL, Hill C, Shorthill RW et al. Atmos Environ 1991;15:2511–9.
[78] Mishchenko MI, Travis LD, Kahn RA, West RA. J Geophys Res 1997;102:16831–47.
[79] West RA, Doose LR, Eibl AM et al. J Geophys Res 1997;102:16871–81.
[80] Muñoz O, Volten H, Rol E et al. Experimental determination of scattering matrices of mineral particles. In: Mishchenko MI, Travis LD, Hovenier JW, editors. Light scattering by nonspherical particles: theory, measurements, and applications. Boston, MA, USA: American Meteorological Society, 1998. p. 265–8.
[81] Hovenier JW, Hage JI. Astron Astrophys 1989;214:391–401.
[82] Joseph JH, Wiscombe WJ, Weinman JA. J Atmos Sci 1976;33:2452–9.
[83] Macke A, Mueller J, Raschke E. J Atmos Sci 1996;53:2813–25.
[84] Mishchenko MI, Rossow WB, Macke A, Lacis AA. J Geophys Res 1996;101:16973–85.
[85] Kokhanovsky A. Optics of light scattering media: problems and solutions. Chichester: Wiley-Praxis, 1999.
[86] Bohren CF, Beschta RL. Cold Reg Sci Technol 1979;1:47–50.
[87] Wiscombe WJ, Warren SG. J Atmos Sci 1980;37:2712–33.
[88] Fraden S, Maret G. Phys Rev Lett 1990;65:512–5.
[89] Kumar S, Tien CL. ASME J Heat Transfer 1990;112:178–85.
[90] Göbel G, Kuhn J, Fricke J. Waves Random Media 1995;5:413–26.
[91] Shinde R. Balgi G, Richter S, Banerjee S, Reynolds J, Pierce J, Sevick-Muraca E. Appl Opt 1999;38:197–204.
[92] Barabanenkov YuN, Kravtsov YuA, Ozrin VD, Saichev AI. Enhanced backscattering in optics. In: Wolf E, editor. Progress in Optics. Vol. XXIX. Amsterdam: Elsevier, 1991. p. 65–197.
[93] Mishchenko MI. JQSRT 1996;56:673–702.
[94] Fung AK, Eom HJ. IEEE Trans Geosci Remote Sens 1985;23:761–7.
[95] Chuah H-T, Tjuatja S, Fung AK, Bredow JW. IEEE Trans Geosci Remote Sens 1996;34:1137–43.
[96] Shepard MK, Campbell BA. Icarus 1998;134:279–91.
[97] Hillier JK. Icarus 1997;130:328–35.

ERRATUM

Equation (43) should read as follows:

$$\mu_p = \cos\left(\frac{\pi}{4}X_p + \frac{\pi}{4}\right), \qquad w_p = \frac{\pi}{4}W_p \sin\left(\frac{\pi}{4}X_p + \frac{\pi}{4}\right), \qquad p = 1, \ldots, n,$$